Characterization of the hairpin vortex solution in plane Couette flow

Sotos C. Generalis*
School of Engineering and Applied Sciences, Mathematics, Aston University, Birmingham B4 7ET, United Kingdom

Tomoaki Itano
Department of Pure and Applied Physics, Faculty of Engineering Science, Kansai University, Osaka 564-8680, Japan
(Received 17 March 2010; revised manuscript received 29 October 2010; published 10 December 2010)

Quantitative evidence that establishes the existence of the hairpin vortex state (HVS) [T. Itano and S. C. Generalis, Phys. Rev. Lett. **102**, 114501 (2009)] in plane Couette flow (PCF) is provided in this work. The evidence presented in this paper shows that the HVS can be obtained via homotopy from a flow with a simple geometrical configuration, namely, the laterally heated flow (LHF). Although the early stages of bifurcations of LHF have been previously investigated, our linear stability analysis reveals that the root in the LHF yields multiple branches via symmetry breaking. These branches connect to the PCF manifold as steady nonlinear amplitude solutions. Moreover, we show that the HVS has a direct bifurcation route to the Rayleigh-Bénard convection.

DOI: 10.1103/PhysRevE.82.066308 PACS number(s): 47.27.Cn, 47.27.De, 47.27.ed

I. INTRODUCTION

In a turbulent boundary layer, the cascade of kinetic energy from the streamwise flow into turbulent internal energy is determined mainly by the intermittent behavior of coherent structures in the shear layer. Moreover, coherent structures are thought to form an integral part of the mechanism that sustains the turbulent states, as well as to contribute to the energy cascade to near-wall turbulence. The influence of the coherent structures on the fully developed turbulent state has, however, never been properly evaluated, partly because of the absence of an exact definition of the notion of coherent structure. Quantitative identification of the coherent structures could be possible via comparison(s) with steady nonlinear amplitude solutions for a wide range of the flow field parameter region.

Theodorsen's proposed hairpin (horseshoe)-shaped vortex [1] as a model of a coherent structure in boundary-layer turbulence has attracted the attention of investigators of turbulent eddy structures. In the absence of dampening effects, hairpin vortex states will generate omega-shaped vortices [2] (see also Ref. [3]) that would gradually dissipate or generate secondary hairpins upstream as well as downstream, depending on the initial energy supplied from the streamwise flow. This process is continual and activates the transportation of momentum in the turbulent boundary, accounting therefore for the observed turbulent Reynolds stresses [4]. It is therefore of great significance to identify the coherent structure, specifically the hairpin-shaped vortex that is prevalent in turbulent shear flow, as a steady nonlinear amplitude solution for a wide range of parameters. The postulate of Ref. [1] will therefore gain support both from laboratory observations and numerical simulations.

A promising candidate of steady nonlinear amplitude solutions corresponding to the hairpin-shaped vortex in plane Couette flow (PCF) was recently presented as hairpin vortex state (HVS) by the authors [5]. In the present paper, we will exhibit quantitative evidence that establishes the existence of the HVS in PCF, qualitative evidence of which was recently elucidated in Ref. [5]. A homotopy continuation from laterally heated flow (LHF) shows that the HVS in PCF has a root in LHF. The early stages of bifurcation of LHF have been investigated previously [6]; but, in the present work, our numerical linear stability analysis reveals that the root in the LHF yields multiple branches via breaking of symmetries. One of the emerging branches corresponds to the HVS in PCF.

We organize the present work as follows. In the following section, Sec. II, we introduce the mathematical formulation in order to obtain the HVS solution in PCF. Here, we introduce a homotopy parameter ϵ, which is not inherent to Couette Flow, but hitherto present at the initial stages of our calculations. In Sec. III we expose step by step the evidence of the bifurcation sequence of branches that evolve from the basic flow in LHF and that lay the foundation of our examination of their connection with PCF. Finally, we present results that show the direct connection of HVS with the Rayleigh-Bénard convection, as well as our concluding remarks in the last section of this paper.

II. FORMULATION

We suppose that the incompressible Newtonian fluid with thermal diffusivity $\tilde{\kappa}$ and kinematic viscosity $\tilde{\nu}$ is confined between two infinite parallel vertical plates, a distance $2\tilde{h}$ apart, which are laterally heated at different temperatures, $\tilde{T} \pm \Delta\tilde{T}$, moving in the opposite directions with velocities $\pm\Delta\tilde{U}$ (see Fig. 1). Assuming that the fluid is under the influence of a uniform vertical gravitational field ($\tilde{g}$ is the acceleration due to gravity), the fluid motion is modeled by the following equations:

$$\tilde{\boldsymbol{\nabla}} \cdot \tilde{\boldsymbol{u}} = 0,$$

$$\tilde{\rho}[\partial_{\tilde{t}}\tilde{\boldsymbol{u}} + (\tilde{\boldsymbol{u}} \cdot \tilde{\boldsymbol{\nabla}})\tilde{\boldsymbol{u}}] = -\tilde{\boldsymbol{\nabla}}\tilde{p} + \tilde{\mu}\tilde{\boldsymbol{\nabla}}^2\tilde{\boldsymbol{u}} - \tilde{\rho}\tilde{g}\boldsymbol{e}_x,$$

*s.c.generalis@aston.ac.uk

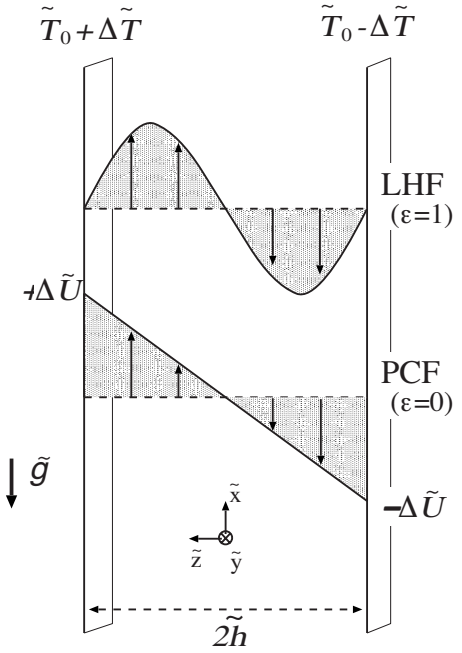

FIG. 1. Geometrical configuration of the fluid flow in a vertical slot between laterally heated boundaries moving in the opposite directions.

$$\partial_{\tilde{t}}\tilde{T}+(\tilde{\boldsymbol{u}}\cdot\tilde{\boldsymbol{\nabla}})\tilde{T}=\tilde{\kappa}\tilde{\boldsymbol{\nabla}}^2\tilde{T},$$

where $\widetilde{(\cdot)}$ indicates a dimensional variable. Here, we restrict ourselves to the state of pure conduction. In this limit the energy equation decouples from the momentum equations and the temperature gradient becomes constant. Taking additionally into account the Boussinesq approximation and the no-slip boundary conditions imposed on the velocity field, the perturbation from the hydrostatic equilibrium is governed by

$$\boldsymbol{\nabla}\cdot\boldsymbol{u}=0,$$

$$\partial_t\boldsymbol{u}+(\boldsymbol{u}\cdot\boldsymbol{\nabla})\boldsymbol{u}=-\frac{1}{\rho_0}\boldsymbol{\nabla}p+\frac{6\epsilon}{\mathrm{Re}}z\boldsymbol{e}_x+\frac{1}{\mathrm{Re}}\boldsymbol{\nabla}^2\boldsymbol{u}.$$

Here, the Reynolds number Re and ϵ are the two nondimensional parameters defined by $\mathrm{Re}=(\tilde{A}+\Delta\tilde{U})\tilde{h}/\tilde{\nu}$ and $\epsilon=\tilde{A}/(\tilde{A}+\Delta\tilde{U})$, where $\tilde{A}=\tilde{\gamma}\tilde{g}\Delta\tilde{T}\tilde{h}^2/6\tilde{\nu}$ and $\tilde{\nu}=\tilde{\mu}/\tilde{\rho}_0$. The variables $\tilde{\gamma}$ and $\tilde{\rho}_0$ are the thermal expansivity and the density, at the reference temperature $\tilde{T}_0$, respectively. The nonslip condition on the rigid boundaries is satisfied if $\boldsymbol{u}(x,y,z=\pm1)=\pm(1-\epsilon)\boldsymbol{e}_x$ and x,y,z are the streamwise, spanwise, and wall-normal directions, respectively, of our coordinate system, which is positioned in the midplane of the layer (see Fig. 1). Assuming the laminar solution to be streamwise directional, we have the basic state $\boldsymbol{u}(z)=(z-\epsilon z^3)\boldsymbol{e}_x$.

The parameter ϵ plays an important role in our analysis. Hereafter, we will explore the composite state of two distinct flow states by varying ϵ in the range $0<\epsilon<1$. The solution obtained with $\epsilon=0$ is the exact state of "pure" PCF, which is driven only by the shear force transferred from the walls moving in the opposite directions; equally, the solution with $\epsilon=1$ is the exact state of pure LHF, which is sustained only by the buoyancy force generated by the temperature difference of the wall boundaries.

We assume that the flow is steady, and that it can be expanded in a double Fourier expansion in the x,y coordinates and in a modified Chebyshev expansion in the z direction:

$$u_j(x,y,z)=\sum_{n_x=-N_x}^{N_x}\sum_{n_y=-N_y}^{N_y}\sum_{n_z=0}^{N_z}\hat{u}_j(n_x,n_y,n_z)\times(1-z^2)^{J(j)}T_{n_z}(z)e^{in_x\alpha x}e^{in_y\beta y},$$

where $T_{n_z}(z)$ is the n_zth-order Chebyshev polynomial and $j=\{x,y,z\}$. The function $J(j)$ takes the value of 1 for $j=\{x,y\}$ and takes the value of 2 for $j=z$. The nonslip boundary condition for each component is automatically satisfied by the factor $(1-z^2)^{J(j)}$. Taking into account the imposed symmetries (detailed later) as well as the continuity equation, a Galerkin-type projection yields quadratic equations for the reduced (truncated) independent set of coefficients of the series. The iterative Newton-Raphson method enables us to determine the solutions of the quadratic equation uniquely.

Moreover, a state for which we examine its stability will be considered to be stable if all $\mathrm{Re}[\sigma]<0$ and unstable if any $\mathrm{Re}[\sigma]>0$, where σ represents an eigenvalue of its spectral linear stability analysis. Here, the growth rate σ for a infinitesimal disturbance,

$$\delta u_j(x,y,z,t)=e^{\sigma t}\sum_{n_x,n_y,n_z}\delta\hat{u}_j(n_x,n_y,n_z)\times(1-z^2)^{J(j)}T_{n_z}(y)e^{in_x\alpha x}e^{in_y\beta y},$$

is calculated by the traditional linear stability theory, based on modal analysis. In the analysis we present the eigenvalues ordered according to their magnitude in the numerical spectra.

III. RESULTS

A. Bifurcation sequence in pure LHF

We begin our exposition by presenting in Fig. 2 the bifurcation sequence of our system in pure LHF ($\epsilon=1$). In this figure, the mean shear rate at the boundary, τ, is adopted as an order parameter to characterize the evolving solutions manifold from our basic state. Interpolating between the eigenvalues of Table I, we calculated that the laminar state in pure LHF becomes unstable against a two-dimensional infinitesimal perturbation with streamwise wave number $\alpha=2$ for $\mathrm{Re}=297.9523$. Note that although the primary bifurcation is supercritical, the secondary state has many folds as it evolves with increasing (or decreasing) strength of nonlinearity. This can be seen in Fig. 2, where it is shown explicitly that the secondary state contains a few branches by turning upon itself several times (the branches are depicted as S1, S2, and S3 in Fig. 2).

According to Ref. [6] we expected to observe the subharmonic tertiary state by increasing the value of Re. In our

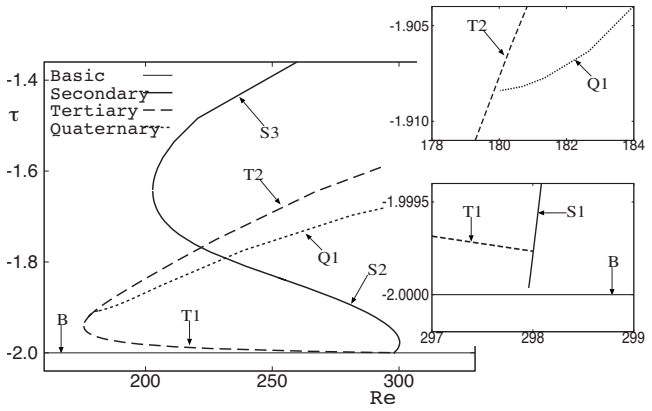

FIG. 2. Bifurcation sequence in pure LHF $\epsilon=1$. The various higher-order states are depicted, as well as the laminar state. The latter is depicted by the line $\tau=-2$. Here, $\epsilon=1$ for the pure LHF states and S, T, and Q stand for secondary, tertiary, and quaternary respectively. The number following each letter indicates the branch of each (bifurcating) state.

case, after the primary bifurcation, the secondary state with $\alpha=2$ looses its stability almost immediately, with the subharmonic instability setting in very quickly. The change of sign for the critical (most dangerous) eigenvalue for two different Re values, one below and one above the bifurcation point of the tertiary state, is given in Table II. This table shows that the secondary instability is indeed monotonic (as the imaginary part of the top eigenvalue vanishes in this case). From linear interpolation based on these eigenvalues, we have identified the bifurcation point of the tertiary state as Re $=298.003$. In our case the bifurcating tertiary state is subcritical (as opposed to the supercritical bifurcation of Ref. [6]) and our subcritical tertiary state evolves with streamwise and spanwise wave numbers $(\alpha,\beta)=(1.0,2.0)$.

As the subcritical tertiary state continues its evolution, it acquires a turning point at Re$=175.64$. Stability analysis tells us that, up to this turning point, the lower branch of tertiary state has several unstable eigenvalues. This implies that several quaternary branches bifurcate from the tertiary state at the Reynolds numbers where the sign of $\mathrm{Re}[\sigma]$ changes. However, of particular interest in the present analysis is the

TABLE I. Eigenvalues indicating bifurcation from the laminar state of pure LHF (see also Fig. 2). The laminar state looses its stability around Re$=297.9528$. Here, we present two sets of eigenvalues σ, one for each of the two values of Re: one below and one above the critical point of the laminar flow. The eigenvalue responsible for the bifurcation presents itself with $\mathrm{Re}[\sigma]>0$.

$\alpha=2.0$, Re$=297.5916$		$\alpha=2.0$, Re$=297.5928$	
$\mathrm{Re}[\sigma]$	$\mathrm{Im}[\sigma]$	$\mathrm{Re}[\sigma]$	$\mathrm{Im}[\sigma]$
-2.8400×10^{-5}	-7.2881×10^{-13}	$+2.0180\times10^{-5}$	-9.2395×10^{-12}
-2.5563×10^{1}	$+2.0670\times10^{2}$	-2.5563×10^{1}	$+2.0670\times10^{2}$
-2.5563×10^{1}	-2.0670×10^{2}	-2.5563×10^{1}	-2.0670×10^{2}
-6.7626×10^{1}	$+1.6691\times10^{2}$	-6.7626×10^{1}	$+1.6691\times10^{2}$
-6.7626×10^{1}	-1.6691×10^{2}	-6.7626×10^{1}	-1.6691×10^{2}

TABLE II. Eigenvalues indicating bifurcation from the supercritical secondary state S1 in pure LHF (see also Fig. 2), with wavenumber values $(\alpha=2.0,\ \beta=0)$. The secondary state S1 looses its stability at Re$=298$. Here, we present two sets of eigenvalues σ for each of the two values of Re: one below and one above the critical point of the secondary state S1. The most dangerous eigenvalue presents itself, as in the case of the laminar flow, with $\mathrm{Re}[\sigma]>0$.

Re$=297.9833$		Re$=298.0167$	
$\mathrm{Re}[\sigma]$	$\mathrm{Im}[\sigma]$	$\mathrm{Re}[\sigma]$	$\mathrm{Im}[\sigma]$
-1.6433×10^{0}	$+8.0632\times10^{-12}$	$+1.1543\times10^{0}$	$+6.6038\times10^{-12}$
-6.9054×10^{0}	$+5.4291\times10^{-10}$	-7.6040×10^{0}	-4.3561×10^{-10}
-9.6752×10^{0}	-4.1537×10^{-10}	-8.9317×10^{0}	$+4.1320\times10^{-10}$
-1.3601×10^{1}	-2.5340×10^{1}	-1.0721×10^{1}	$+2.7901\times10^{1}$
-1.3601×10^{1}	$+2.5340\times10^{1}$	-1.0721×10^{1}	-2.7901×10^{1}

quaternary state that bifurcates from the upper branch at Re≈180. We observe this particular supercritical bifurcation in the change of eigenvalues as given in Table III. The set given in Table III is part of a larger set with additional eigenvalues that are positive, indicating that the upper branch is unstable. The top eigenvalue listed in Table III is responsible for the bifurcation of the quaternary state Q1. Again, in accordance with our previous practice, we provide eigenvalues prior and after the bifurcation point of Q1. Note that there is a pair of complex conjugate eigenvalues included in Table III which do not undergo a Hopf bifurcation until higher Re values.

B. Homotopy between LHF and PCF

Several distinct states at Re$=300$ in LHF $(\epsilon=1)$ have been calculated. For the sake of convenience and reference hereafter, we will denote each state as follows (see also Fig. 2): (B) the basic state; (S1) the lower branch, (S2) the middle branch, and (S3) the upper branch of the secondary state; (T1) the lower branch and (T2) the upper branch of the tertiary state; (Q1) the upper branch and (Q2) the lower branch of the quaternary state.

TABLE III. Eigenvalues indicating bifurcation from the upper branch (T2) of the subcritical tertiary state in pure LHF $(\alpha=1.0,\ \beta=2.0)$ of Fig. 2. The tertiary vortex state looses its stability at around Re$=179.667$. Here, we present two sets of eigenvalues σ for each of the two values of Re: one below and one above the critical point for the tertiary flow in pure LHF $(\epsilon=1)$. The most dangerous eigenvalue presents itself, as before, with $\mathrm{Re}[\sigma]>0$.

Re$=179.667$		Re$=179.833$	
$\mathrm{Re}[\sigma]$	$\mathrm{Im}[\sigma]$	$\mathrm{Re}[\sigma]$	$\mathrm{Im}[\sigma]$
-2.5352×10^{-3}	$+5.8246\times10^{-14}$	$+1.1627\times10^{-3}$	-8.3378×10^{-13}
-2.4033×10^{-2}	-4.3817×10^{-14}	-2.5465×10^{-3}	$+1.4992\times10^{-13}$
-2.0261×10^{0}	-3.9307×10^{0}	-2.0304×10^{0}	-3.9873×10^{0}
-2.0261×10^{0}	$+3.9307\times10^{0}$	-2.0304×10^{0}	$+3.9873\times10^{0}$
-2.6072×10^{0}	$+4.5708\times10^{-14}$	-2.6083×10^{0}	$+8.5950\times10^{-11}$

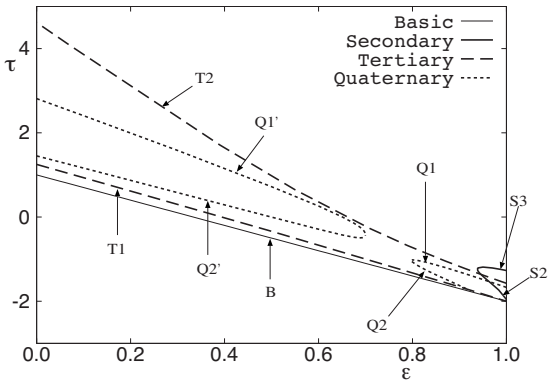

FIG. 3. Bifurcation diagram for Re=300. Several states obtained in LHF show their connections to PCF via the homotopy parameter ϵ. Here, the various states are denoted in the same way as in Fig. 2.

These solutions can now be adopted as seeds to explore previously unknown solutions in PCF via gradually limiting the value of the homotopy parameter ϵ to zero. The connection of these solutions via ϵ is shown in Figs. 3 and 4. In these plots, the basic solution is analytically represented as $\tau=1-3\epsilon$ for any Re. The secondary states in LHF have turning points at $\epsilon>0.9$ in both figures. Although we calculated the turning points of the secondary state in LHF at higher Reynolds numbers, the secondary states were never able to intersect the $\epsilon=0$ plane, a value of ϵ which corresponds to pure PCF. For example, the secondary state at Re=1800 has a turning point at $\epsilon\approx0.8$.

By contrast, the tertiary and quaternary states in LHF can connect with PCF ($\epsilon=0$), as can been seen in Figs. 3 and 4. The tertiary state (with branches T1 and T2), which bifurcated from the secondary state of LHF (see Fig. 2), connects directly with the pure PCF as depicted in Figs. 3 and 4. In particular, it is interesting to note that T2 at PCF shows relatively high value of τ, an attribute that will be discussed later in conjunction with the existing literature. Concentrating on Fig. 4 (where Re=350), the quaternary branches Q1 and Q2 emanate from the two distinct manifolds in the homotopy space, $\epsilon=0$ (PCF) and $\epsilon=1$ (LHF), and show converging tendencies. In fact the connection between LHF and PCF states is achieved at high Re values at the quaternary level. It should be emphasized that the continuous connection of the

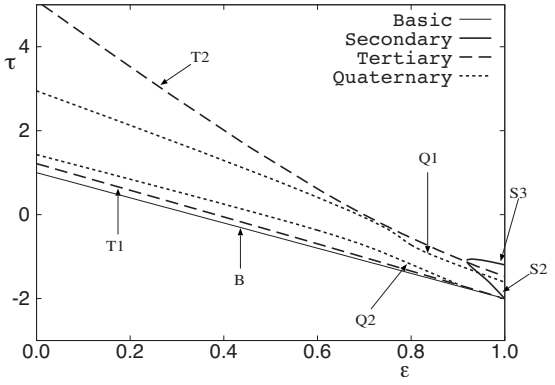

FIG. 4. Bifurcation diagram obtained at Re=350. Here, the various states are denoted in the same way as in Fig. 2.

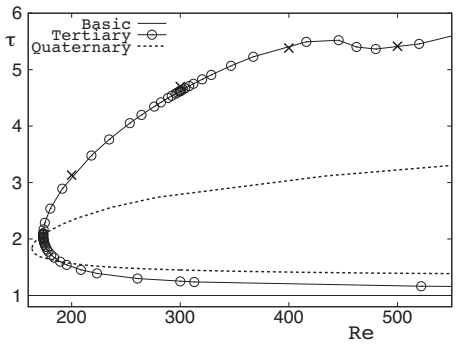

FIG. 5. The tertiary and quaternary states connected to PCF. The value of τ of tertiary state is calculated by two sets of truncation levels, ○: $(N_x,N_y,N_z)=(8,8,28)$ and ×: (32, 16, 60), in order to explicitly show the numerical convergence, necessary for the (absolute) existence of the state.

quaternary states in LHF with the PCF manifold for Re =350 is actually achieved with no symmetry change in the states. We note here additionally that because T1 bifurcates subcritically from S1 in LHF ($\epsilon=1$), the connection with PCF ($\epsilon=0$), which is computationally continuous for all values of the homotopy parameter, is possible only via the upper branch T2, which is the only tertiary branch that exists for $\mathrm{Re}\geq300$ (see Figs. 2 and 3).

The bridge, however, the bridge between PCF and LHF that is made by the quaternary state that originates from LHF, disappears for values of the homotopy parameter ϵ, such that the inequality $0.7<\epsilon<0.8$ is satisfied at lower Re values (see Fig. 3). We confirmed that this separation between the two regions happens below $\mathrm{Re}\approx310$. It is precisely for this reason that one would have failed in attempting to seek a new solution in PCF from known nontrivial solutions of PCF via a homotopy transformation at relatively lower Re values. In some sense therefore the intensity of the inflection point, which increases with increasing Re values (see Ref. [5]), would have been required to build the passage to the new solutions in PCF. This separation may provide also a possible explanation as to why the quaternary state in PCF with $\mathrm{Re}_{\mathrm{min}}=127.705$ (see Ref. [7]) survives for lower Re values than the tertiary state in PCF with $\mathrm{Re}_{\mathrm{min}}=139$ does, in spite of the fact that the latter is a more primitive state than the former in the bifurcation sequence.

C. Bifurcation in PCF

In Ref. [5], the tertiary state connected to PCF was denoted as HVS associated to the shape of hairpin visualized by its vortex lines. The shape of the vortex is attributed to the spanwise reflection symmetry of this state.

In the present study, we have pursued the HVS for both higher and lower Reynolds number values. The calculation has been complied for the upper and lower branches independently with truncation levels such that the numerical tolerance levels were within a preset criterion. The value of τ of the upper branch is captured by various truncation levels in a consistent way, with the calculations depicted within the 1–2 % tolerance range (see Fig. 5). Although the calculation

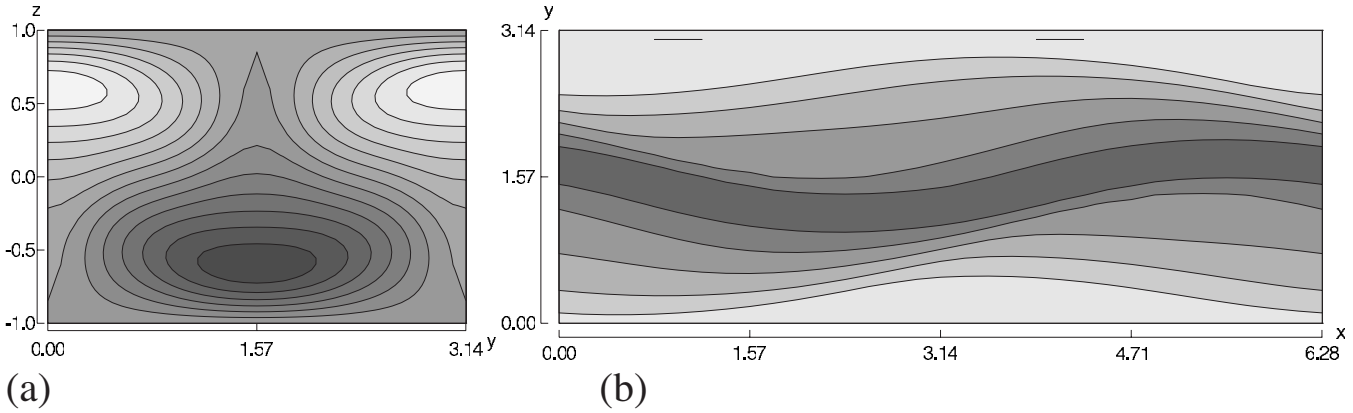

FIG. 6. The quaternary state Q1 at $(\epsilon,\mathrm{Re})=(0,200)$. (a) Contour plot of $\bar{u}(y,z)$, which varies from −0.59 to 0.59. Contour levels from −0.6 (white) to 0.6 (black) by 0.1. (b) Contour plot of $u_+(x,y)$, which varies from 0 to 0.54. Contour levels from 0.0 (white) to 0.6 (black) by 0.1.

of the upper branch proceeds in a consistent manner up to Re=400 with the truncation levels employed, above Re =400 there is a genuine difficulty in obtaining a convergence in accordance with the tolerance criteria set. This necessitates the introduction of higher truncation levels with increasing Re values. The turning point of the HVS for $(\alpha,\beta)=(1,2)$ is $\mathrm{Re}_{\min}=173.79$ for $(N_x,N_y,N_z)=(8,8,28)$ and $\mathrm{Re}_{\min}=173.98$ for $(N_x,N_y,N_z)=(16,16,28)$, where (N_x,N_y,N_z) constitutes the truncation level in the streamwise, spanwise, and wall-normal coordinates, respectively. The upper branch, of the tertiary state that connects to PCF for the same wave numbers, has $\mathrm{Re}_{\min}=163.5$ for $(N_x,N_y,N_z)=(8,16,28)$, which is in accordance with Ref. [8]. The turning point of the HVS can be optimized with varying (α,β), where $\mathrm{Re}_{\min}=139.2$ is achieved for $(\alpha,\beta)=(0.757,1.366)$ in the present investigation with $(N_x,N_y,N_z)=(8,8,28)$.

On the other hand, the lower branch can be pursued at relatively less truncation levels, because the streamwise dependency of the lower branch is relatively small. This is similar to the lower branch of the quaternary state, which was the focus of Ref. [8].

IV. CONCLUSIONS AND DISCUSSION

We have exposed the method employed to identify another family of solutions to the Navier-Stokes equations in PCF. In Ref. [5], the solutions found were classified by symmetries into the HVS and a previously identified solution, which was abbreviated as NBW (from Nagata, Clever & Busse, Waleffe). Indeed, the HVS is intrinsically more complicated than NBW, despite the fact that it satisfies richer symmetries than it does. In the present study, we have also explicitly shown that the latter bifurcates from the former.

A. Symmetry considerations

We review now the bifurcation sequence from the symmetries point of view. The following symmetries are satisfied by the tertiary state [5]:

($\mathcal{A}$) Streamwise translational and spanwise reflectional symmetry, $[u_x,u_y,u_z]^T(x,y,z)=[u_x,-u_y,u_z]^T(x+L_x/2,-y,z)$;

($\mathcal{B}$) Parity symmetry with respect to $(x,y,z)=(L_x/4,L_y/4,0)$, $[u_x,u_y,u_z]^T(x,y,z)=[-u_x,-u_y,-u_z]^T(L_x/2-x,L_y/2-y,-z)$; and

($\mathcal{C}$) Parity symmetry with respect to the origin, $[u_x,u_y,u_z]^T(x,y,z)=[-u_x,-u_y,-u_z]^T(-x,-y,-z)$.

Denoting by $\mathcal{T}_{\Delta x,\Delta y}$ the translational symmetry in the streamwise and spanwise directions, $[u_x,u_y,u_z]^T(x,y,z)=[u_x,u_y,u_z]^T(x+\Delta x,y+\Delta y,z)$, we can deduce that the present tertiary state obtained for $(\alpha,\beta)=(1,2)$ is invariant under an arbitrary combination of the noncommunicative operations,

$$\{1,\mathcal{A}^{n_1},\mathcal{B}^{n_2},\mathcal{C}^{n_3},\mathcal{T}_{2\pi,0}^{n_4},\mathcal{T}_{0,\pi}^{n_5}\},$$

where n_i is an arbitrary integer. We note here that the spanwise reflection symmetry with respect to the $y=L_y/4$ plane, $[u_x,u_y,u_z]^T(x,L_y/4+y,z)=[u_x,u_y,u_z]^T(x,L_y/4-y,z)$, can be deduced from $\mathcal{T}_{0,\pi}\mathcal{ABC}$. In addition, we also note that $\mathcal{A}^2=\mathcal{T}_{2\pi,0}$.

In the hierarchical bifurcation sequence, a quaternary state bifurcates from a tertiary state by the breaking of a symmetry, symmetry $\mathcal{C}$ in our case which leads to the breaking of the spanwise reflection symmetry. It should be noted that this symmetry breaking also triggers a significant difference at PCF in vortex structure between HVS and NBW. As seen from the contour plots of $\bar{u}(y,z)$ in Figs. 6 and 7, two streamwise-averaged (absolute value) vorticity peaks are located at $z<0$ and $z>0$ for the tertiary state T2, while only one peak is located at $z=0$ for the quaternary state Q1. Thus, in spite of the fact that these solutions are homotopically equivalent to others in LHF, one is distinct from the other in PCF, in the fact that their own identities are being rooted at a symmetry breaking.

B. Available literature

A very recent compilation of solution space in PCF is by Gibson *et al.* [9]. They employed an algorithm that is based on the Chebyshev tau method, allowing therefore for corrections due to the incompressibility and boundary conditions.

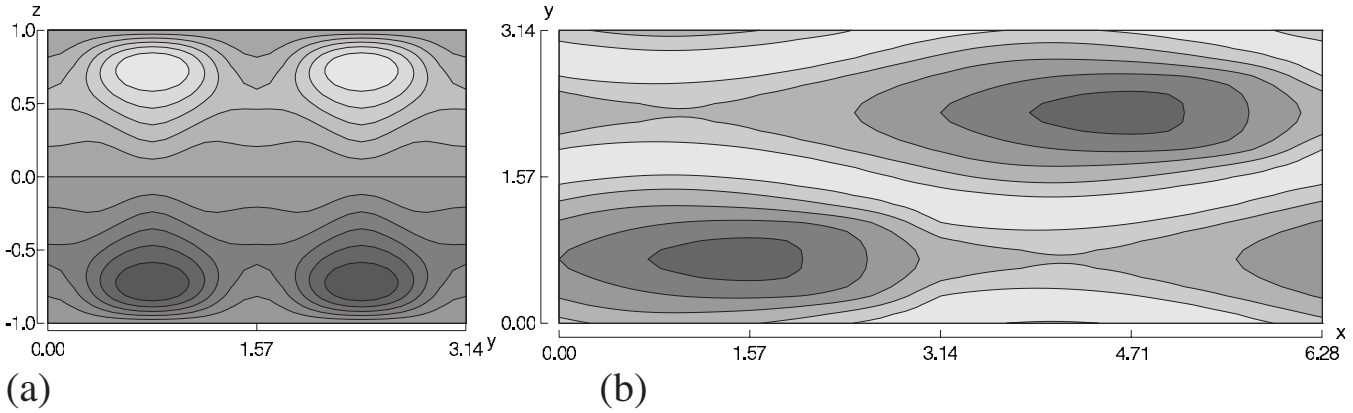

FIG. 7. The tertiary state T2 at $(\epsilon,\mathrm{Re})=(0,200)$. (a) Contour plot of $\bar{u}(y,z)$, which varies from −0.67 to +0.67. Contour levels from −0.7 (white) to 0.7 (black) by 0.1. (b) Contour plot of $u_+(x,y)$, which varies from 0 to 0.59. Contour levels from 0.0 (white) to 0.6 (black) by 0.1.

The spectral resolution employed was sufficient to independently identify the HVS in PCF, despite the quoted low aspect ratio of their computational domain. Among the plethora of states in PCF identified in Ref. [9], their EQ_7 and EQ_8 equilibria are the ones that correspond to the lower and upper branches of the HVS identified in Ref. [5]. The τ, energy, and energy dissipation values for the upper and lower branches of the HVS and EQ_7, EQ_8 of Ref. [9] were compared for a variety of values of Re (see Ref. [10]). The agreement between the two sets of values reported in the above references is excellent.

The work of Schmiegel [11] is also an investigation in the steady and traveling-wave solutions in PCF. Due to the nondimensionalization employed in Ref. [11], where the streamwise and spanwise extent of the periodical computational domain is exactly double of those used in Ref. [5], we should have been able to make direct comparisons. Contour plots of $\bar{u}(y,z)$ and $u_+(x,y)$ are made in order to identify the streak structures of T2 (Fig. 7) and Q1 (Fig. 6) at $(\epsilon,\mathrm{Re})=(0,200)$, where

$$\bar{u}(y,z)=\frac{1}{L_x}\int_0^{L_x} u(x,y,z)-z dx,$$

$$u_+(x,y)=\int_{-1}^{1}[u(x,y,z)-z]\Theta(u(x,y,z)-z)dz,$$

and $\Theta(s)$ is the Heaviside function. Comparing Fig. 6 and $\mathrm{Re}_{\mathrm{min}}$, we conjecture that Q1 is likely to be equivalent to the "α branch" of Ref. [11], except for the difference in the number of streaks. Search for the optimal wave number for Q1, where the state can exist for the lowest value of the Reynolds number, gives us a good accordance in the value of $\mathrm{Re}_{\mathrm{min}}$ of Q1. On the other hand, by comparing Fig. 7 and taking into account the symmetries satisfied (and the relatively high value of τ of T2), T1 or T2 appears to be similar to the σ branch in Ref. [11], except for the quantitative significant differences in $\mathrm{Re}_{\mathrm{min}}$ and τ. We find that the difference between the two studies is large even at relatively lower Reynolds number values. We believe that is probably caused by the low truncation levels of Ref. [11], despite the fact that Legendre and not Chebyshev polynomials are employed there. We are thus unable to make a fully convincing comparison with Ref. [11].

C. Connection of HVS to Rayleigh-Bénard convection

Clever and Busse [12,13] introduced PCF between horizontal boundaries at different temperatures (conventional Rayleigh-Bénard convection: RBC) to reproduce the NBW. This NBW was identified as a tertiary branch in Ref. [12], because this branch bifurcates directly from the two-dimensional solution. In order to examine the bifurcation diagram of HVS in the homotopy space between PCF and RBC, we carried out extra calculations.

At first, we summarize here their result very briefly (basing our analysis on Fig. 1 of Ref. [13]). At the critical Rayleigh number $\mathrm{Ra}\approx 1708/16=106.7$, where the basic flow loses its stability, the two-dimensional flow (*longitudinal roll cell* in RBC) emerges from the basic flow. Note that each roll cell in this secondary flow occupies the whole channel width. Then the wavy instability of the roll cell leads to a three-dimensional flow (the tertiary branch in their sense), which can be realized even in the vanishing limit of Ra, corresponding to NBW in pure PCF. Despite the fact that there are two control parameters only one of them was used here, Ra, that provides the *degeneracy* prevailing in the horizontal configuration, when $\Delta U\to 0$. This arbitrariness in the direction of axes of the roll cells on the horizontal plane in pure RBC due to isotropy invariance, aided by the vanishing of ΔU, allows even for square and hexagonal patterns to be realized with a subtle modification of the flow pattern, which would be very important for other possible extension of bifurcations.

In Fig. 8 we show the bifurcation diagram of HVS in homotopy between HVS and RBC. For this figure,

$$L_2=\sum_{n_x=-N_x}^{N_x}\sum_{n_y=-N_y}^{N_y}\sum_{n_z=0}^{N_z}[\hat{u}_j(n_x,n_y,n_z)\hat{u}_j(n_x,n_y,n_z)^*],$$

where $*$ in this expression refers to the complex conjugate. In RBC the main results available in the literature are derivable from the bifurcation sequence of the even mode, as the

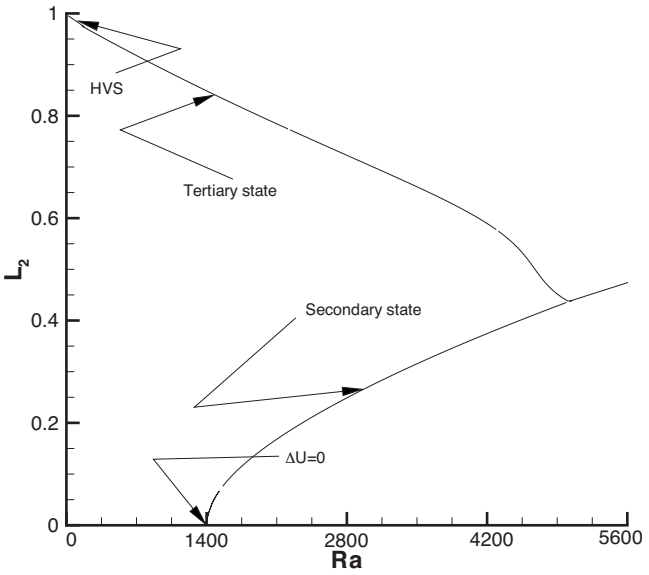

FIG. 8. Bifurcation in thermally stratified PCF. The vertical axis denotes the L_2 norm of the vertical component of the velocity field. The bifurcation diagram is obtained in thermally stratified PCF. The secondary flow corresponds to longitudinal roll cells. Here, the Re and Prandtl numbers are kept fixed at 210 and 7, respectively. The Rayleigh number value Ra$\approx$1403 is the critical value in RBC for the odd mode.

odd mode has a higher critical Rayleigh number. When thermal effects are introduced in the PCF, the nonlinear odd mode bifurcates at Ra$\approx$1403 for the wave-number value α =4, precisely as predicted from the corresponding linear analysis. As the nonlinear states are followed in the nonlinear space a subharmonic subcritical bifurcation occurs at Ra $\approx$4991, creating the predecessor of the HVS in PCF, with the wave-number values presented in this work.

As can be seen from Fig. 8, when the thermal effects are then gradually removed we reach the case of PCF and the previously identified HVS is obtained again. By eliminating therefore RBC we are able to obtain the HVS in PCF via another route. The consideration of the bifurcation sequence of the odd mode in RBC provides therefore another connection to the HVS manifold of solutions. Thus, the attempts of Ref. [13] could not connect to HVS, because their hierarchical bifurcations originated from a different mode, the even one.

ACKNOWLEDGMENTS

We are both grateful to Professor Gibson for sharing with us numerical data that enabled us to compare our results with the results of his group. T.I. is grateful for the financial support received from Aston University under the Visiting Scholars Fund Scheme and EPSRC (Contract No. GR/S70593/01), which allowed him to spend time in the United Kingdom, while working on this project. S.C.G. is grateful for a Research Invitation from the Kansai University, which allowed him to spend time in Japan during the final stages of this work. This work was also supported in part by KAKENHI (Contract No. 19760123) and by the Kansai University Special Research Fund 2009 and 2010.

[1] T. Theodorsen, Proceedings of the Second Midwestern Conference on Fluid Mechanics, 1952 (unpublished), pp. 1–19.
[2] S. K. Robinson, Annu. Rev. Fluid Mech. **23**, 601 (1991).
[3] R. J. Adrian, Phys. Fluids **19**, 041301 (2007).
[4] A. E. Perry and I. Marusic, J. Fluid Mech. **298**, 361 (1995).
[5] T. Itano and S. C. Generalis, Phys. Rev. Lett. **102**, 114501 (2009).
[6] M. Nagata and F. Busse, J. Fluid Mech. **135**, 1 (1983).
[7] F. Waleffe, Phys. Fluids **15**, 1517 (2003).
[8] J. Wang, J. Gibson, and F. Waleffe, Phys. Rev. Lett. **98**, 204501 (2007).
[9] J. F. Gibson, J. Halcrow, and P. Cvitanovic, J. Fluid Mech. **638**, 243 (2009).
[10] J. F. Gibson (private communication).
[11] A. Schmiegel, Ph.D. thesis, Philipps-Universität Marburg, 1999.
[12] R. M. Clever and F. H. Busse, J. Fluid Mech. **234**, 511 (1992).
[13] R. M. Clever and F. H. Busse, in *Physics of Rotating Fluids*, Lecture Notes in Physics Vol. 549, edited by C. Egbers and G. Pfister (Springer, New York, 2000), pp. 399–416.